The Astrophysical Journal, 860:149 (14pp), 2018 June 20 https://doi.org/10.3847/1538-4357/aac267

Constraining the Speed of Sound inside Neutron Stars with Chiral Effective Field Theory Interactions and Observations

I. Tews[1,2], J. Carlson[3], S. Gandolfi[3], and S. Reddy[1,2]
[1] Institute for Nuclear Theory, University of Washington, Seattle, WA 98195-1550, USA; itews@uw.edu
[2] JINA-CEE, Michigan State University, East Lansing, MI, 48823, USA; sareddy@uw.edu
[3] Theoretical Division, Los Alamos National Laboratory, Los Alamos, NM 87545, USA; carlson@lanl.gov, stefano@lanl.gov
Received 2018 January 16; revised 2018 April 30; accepted 2018 May 1; published 2018 June 21

Abstract

The dense matter equation of state (EOS) determines neutron star (NS) structure but can be calculated reliably only up to one to two times the nuclear saturation density, using accurate many-body methods that employ nuclear interactions from chiral effective field theory constrained by scattering data. In this work, we use physically motivated ansatzes for the speed of sound c_S at high density to extend microscopic calculations of neutron-rich matter to the highest densities encountered in stable NS cores. We show how existing and expected astrophysical constraints on NS masses and radii from X-ray observations can constrain the speed of sound in the NS core. We confirm earlier expectations that c_S is likely to violate the conformal limit of $c_S^2 \leqslant c^2/3$, possibly reaching values closer to the speed of light c at a few times the nuclear saturation density, independent of the nuclear Hamiltonian. If QCD obeys the conformal limit, we conclude that the rapid increase of c_S required to accommodate a $2\,M_\odot$ NS suggests a form of strongly interacting matter where a description in terms of nucleons will be unwieldy, even between one and two times the nuclear saturation density. For typical NSs with masses in the range of 1.2–1.4 $M_\odot$, we find radii between 10 and 14 km, and the smallest possible radius of a $1.4\,M_\odot$ NS consistent with constraints from nuclear physics and observations is 8.4 km. We also discuss how future observations could constrain the EOS and guide theoretical developments in nuclear physics.

Key words: dense matter – equation of state – stars: neutron

1. Introduction

The neutron-matter equation of state (EOS) at $T = 0$ is a crucial ingredient to describe the structure of neutron stars (NS), as expressed by the mass–radius relation. At the high densities in the NS core, the proton fractions are small, typically 5%–10%, and NS matter can be effectively described as pure neutron matter (PNM). Although protons are included when constructing the EOS of NSs, their contribution is small (compared to other uncertainties, which we shall discuss in some detail) and always acts to reduce the pressure. Up to ∼1–2 times the nuclear saturation density, $n_0 = 0.16\,\mathrm{fm}^{-3} \simeq 2.7 \cdot 10^{14}\,\mathrm{g\,cm}^{-3}$, the EOS of PNM has been computed by using different many-body methods with realistic nucleon–nucleon interactions; see, e.g., Hebeler & Schwenk (2010), Gandolfi et al. (2012, 2015), Tews et al. (2013), Hagen et al. (2014), Sammarruca et al. (2015), Lynn et al. (2016), Drischler et al. (2016), and Holt & Kaiser (2017). In the following, we shall collectively refer to them as ab initio calculations. At densities above $2n_0$, however, the PNM EOS is not constrained.

From the EOS, $p = p(\epsilon)$, we can obtain the speed of sound c_S from

$$c_S^2 = \frac{\partial p(\epsilon)}{\partial \epsilon}, \tag{1}$$

with the pressure p and the energy density ϵ, where the latter also includes the rest-mass contribution. Stability and causality constrain $0 \leqslant c_S^2 \leqslant 1$, where we have set the speed of light $c = 1$. Current ab initio calculations of neutron matter constrain the speed of sound up to ≈1–$2n_0$, but, again, at higher densities uncertainties grow rapidly and the speed of sound remains unconstrained.

In this work, we show that useful constraints on the speed of sound at higher densities can be deduced from the observation of two-solar-mass NS (Demorest et al. 2010; Antoniadis et al. 2013) by using ab initio calculations of the EOS of PNM up to 1–$2n_0$. Our work is similar in some respects to earlier work by Bedaque & Steiner (2015), where c_S at high density was constrained using a parameterized EOS and astrophysical observations. An important distinction is that we use ab initio methods and nuclear interactions from chiral effective field theory (EFT) which allows us to study the influence of uncertainties due to poorly constrained short-distance behavior of two- and three-nucleon interactions.

At very high densities, far exceeding the densities in the NS core, additional information on the speed of sound can be obtained from perturbative QCD. These calculations of cold ultra-dense quark matter, which are reliable at asymptotic density, show that corrections due to interactions between quarks decrease c_S and that $c_S^2 < 1/3$ (Kurkela et al. 2010). They also show that $c_S^2 \to 1/3$ with increasing density from below. In general, in conformal theories, where the trace of the energy momentum tensor $\epsilon - 3P$ vanishes, $c_S^2 = 1/3$ is independent of density, temperature, or interactions. Lattice QCD calculations at finite temperature and zero chemical potential show that $c_S^2 < 1/3$, and that the introduction of a small baryon chemical potential does not alter this result (Borsanyi et al. 2012). The speed of sound has also been calculated in a large class of theories for which the ADS/CFT correspondence holds, and calculations are possible in the strong coupling limit. It has been conjectured that $c_S^2 < 1/3$, even when the trace of the energy momentum tensor is nonzero (Cherman et al. 2009), although recently explicit counter-examples have been presented (Hoyos et al. 2016;

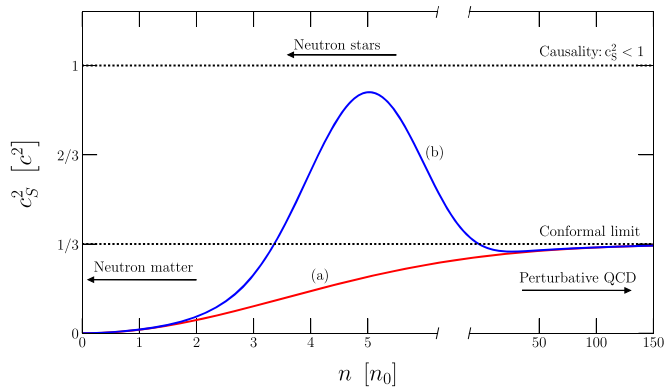

Figure 1. Two possible scenarios for the evolution of the speed of sound in dense matter.

Ecker et al. 2017). We refer the reader to Bedaque & Steiner (2015) for a more detailed discussion of this conjecture and known exceptions (see also Hoyos et al. 2016 and Ecker et al. 2017).

For QCD at finite baryon density, we are unaware of compelling reasons to expect that $c_S^2 < 1/3$, and based on the preceding arguments, we will consider two minimal scenarios, which are illustrated in Figure 1. The scenario labeled (a) corresponds to the case when we assume that QCD obeys the conformal limit $c_S^2 < 1/3$ at all densities, and scenario (b) corresponds to QCD violating this conformal bound. The behavior of c_S at low and high density is constrained by theory, and we shall show that NS observations, when combined with improved ab initio calculations of PNM, can distinguish between these two scenarios, and provide useful insights about matter at densities realized inside NSs.

This paper is structured as follows. In Section 2, we present constraints on the speed of sound from nuclear physics. In Section 3, we extend the speed of sound to higher densities. In Section 3.1, we study the EOS under the assumption that the conformal limit is obeyed and the speed of sound is bounded by $1/\sqrt{3}$. For this case, we find that c_S needs to increase very rapidly above 1–2n_0 to stabilize a $2\,M_\odot$ NS. Such a rapid increase likely signals the appearance of a new form of strongly coupled matter where the nucleon is no longer a useful degree of freedom. In Section 3.2, we release this assumption but still find that models in which c_S increases rapidly, reaching values close to c, are favored. We study correlations in our parameterization in Section 3.3. In Section 4, we derive the smallest possible radius for NSs consistent with nuclear physics and observations. We then investigate the impact of possible additional observations in Section 5. Finally, we summarize our main findings in Section 6.

2. EOS and Speed of Sound from Nuclear Physics

2.1. The EOS of Neutron Matter

In this work, we use auxiliary-field diffusion Monte Carlo (AFDMC) to find the many-body ground state for a given nonrelativistic nuclear Hamiltonian (Carlson et al. 2015). In general, the nuclear Hamiltonian contains two-body (NN), three-body (3N), and higher many-body (AN) forces,

$$\mathcal{H} = \mathcal{T} + \mathcal{V}_{\rm NN} + \mathcal{V}_{\rm 3N} + \mathcal{V}_{\rm AN}, \tag{2}$$

which can be obtained from chiral effective field theory (EFT) at low-density (see, for instance, Epelbaum et al. 2009 and Machleidt & Entem 2011). Chiral EFT is a systematic framework for low-energy hadronic interactions, that naturally includes both two-body and many-body forces and allows for systematic uncertainty estimates. It has been successfully used to calculate nuclei and nuclear matter, see, for instance, Hebeler et al. (2015) and references therein.

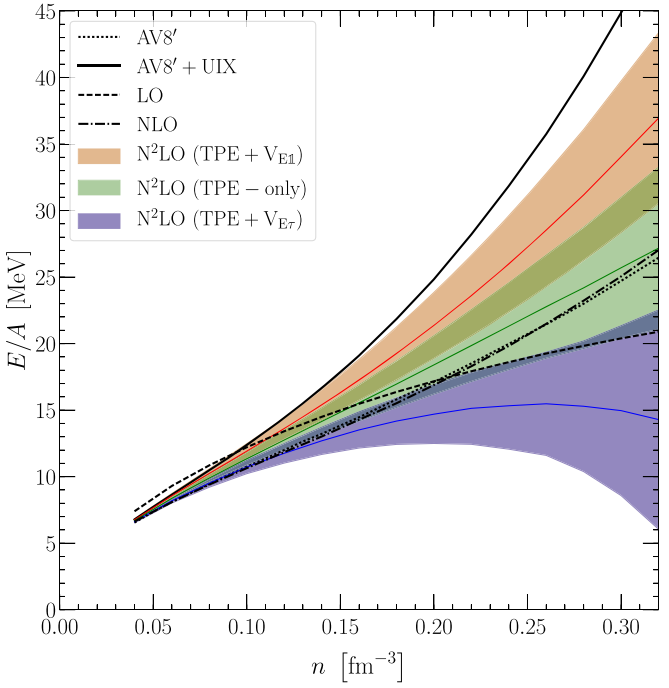

Figure 2. Neutron-matter EOSs used in this work. We show the AFDMC results for local chiral Hamiltonians with three different 3N short-range operators: TPE-only (green middle band), TPE+$V_{E,\mathbb{1}}$ (red upper band), and TPE+$V_{E,\tau}$ (blue lower band), see Lynn et al. (2016) for details. For comparison, we also show results for the phenomenological AV8′+UIX interactions (black line), for AV8′ (dotted line), as well as LO (dashed line) and NLO (dashed–dotted line) results for the local chiral interactions of Gezerlis et al. (2014) with $R_0 = 1.0$ fm.

In this paper, we extend the AFDMC calculations of PNM of Lynn et al. (2016) with recently developed local chiral N^{2}LO interactions, including two- and three-body forces of Gezerlis et al. (2013, 2014) and Tews et al. (2016), to higher densities. We find that, despite the rapid increase of the error estimates, EFT-based interactions remain useful up to $n = 0.32$ fm^{-3} and our results for the energy per particle in neutron matter are shown in Figure 2. We plot the results for local chiral interactions at LO, NLO, and N^{2}LO with three different 3N interactions defined in Lynn et al. (2016): 3N interactions with only the two-pion exchange (TPE-only), and 3N interactions containing the TPE plus shorter-range contact terms with two different spin-isospin operators (TPE + $V_{E,\mathbb{1}}$ and TPE + $V_{E,\tau}$), see Lynn et al. (2016) for details. The uncertainty bands for the individual N^{2}LO interactions are obtained as suggested by Epelbaum et al. (2015), i.e., the uncertainty $\Delta X^{\rm N^2LO}$ at order N^{2}LO is given by

$$\Delta X^{\rm N^2LO} = \max\left(Q^4|X^{\rm LO} - X^{\rm free}|,\ Q^2|X^{\rm NLO} - X^{\rm LO}|,\ Q|X^{\rm N^2LO} - X^{\rm NLO}|\right), \tag{3}$$

and similar for lower orders. The dimensionless expansion parameter Q is given by $Q = \max(p/\Lambda_B, m_\pi/\Lambda_B)$ with p being

Table 1
Energy per Particle and Pressure in PNM at n_0 and $2n_0$ for Local Chiral Hamiltonians

		Free	Pheno.	LO	NLO	N^{2}LO (TPE-only)	N^{2}LO ($+V_{E,\mathbb{1}}$)	N^{2}LO ($+V_{E,\tau}$)
E/A	n_0	35.1	19.1	15.5 ± 5.2 (8.6)	14.3 ± 2.7 (5.7)	15.6 ± 1.4 (3.8)	17.3 ± 1.5 (3.8)	13.5 ± 1.4 (3.8)
	$2n_0$	55.7	49.9	20.9 ± 14.6 (24.3)	27.0 ± 9.4 (20.3)	27.2 ± 6.1 (16.9)	36.9 ± 6.4 (16.9)	14.3 ± 8.2 (16.9)
P	n_0	3.7	3.3	1.3 ± 0.7 (1.1)	1.6 ± 0.4 (0.8)	1.8 ± 0.2 (0.5)	2.4 ± 0.4 (0.6)	1.1 ± 0.3 (0.5)
	$2n_0$	11.9	25.8	3.1 ± 3.7 (6.1)	9.8 ± 4.4 (5.6)	7.8 ± 2.8 (4.7)	15.1 ± 3.4 (4.7)	−2.6 ± 8.1 (10.4)

Note. Energy per particle and pressure in PNM at n_0 and $2n_0$ for local Chiral Hamiltonians at LO, NLO, and N^{2}LO with three different short-range operators. The uncertainties are obtained using Equation (3) with two different expansion parameters p/Λ_B with $p = \sqrt{3/5}\,k_F$ and $p = k_F$ in parenthesis. We also give the values for the free Fermi gas and the phenomenological AV8′+UIX interaction.

a typical momentum scale of the system, m_π being the pion mass, and $\Lambda_B \approx 500$ MeV being the breakdown scale of chiral EFT. For PNM in Figure 2, we use the scale $p = \sqrt{3/5}\,k_F$; see Lynn et al. (2017). The results indicate that the EOS of PNM is well constrained up to saturation density, but the associated error grows rapidly with density. Nonetheless, the order-by-order convergence is still consistent with EFT expectations in the range $n_0 - 2n_0$. In addition, although these interactions are only fit to low-energy scattering data up to laboratory energies of 150 MeV, they also describe phase shifts at much higher energies within uncertainties; see, e.g., Epelbaum et al. (2015). For comparison, we also show results obtained using the phenomenological Argonne v8′ NN interaction (AV8′) and the Urbana IX 3*N* interactions (UIX) in Figure 2.

We present the energy per particle and the pressure at n_0 and $2n_0$ at LO, NLO, and N^{2}LO in Table 1 to provide supporting arguments for the convergence of the chiral expansion in this density range. Uncertainty estimates in Table 1 are provided by assuming a typical momentum scale $p = \sqrt{3/5}\,k_F$ and, in addition, a more conservative choice $p = k_F$. At saturation density, we find a systematic order-by-order convergence for both energy and pressure: the results at different orders overlap within their uncertainties, which decrease order-by-order.

From Figure 2 and Table 1, we see that the shorter-range 3*N* interactions significantly influence the convergence, but are still within conservative uncertainty estimates. These shorter-range 3*N* forces appear at N^{2}LO in the chiral power counting and contribute to systems containing triples of both neutrons and protons with $S = 1/2$ and $T = 1/2$, where S and T are the total spin and isospin, respectively. They are typically fit to few-body observables, such as the ^{4}He binding energy and neutron-alpha scattering (see Lynn et al. 2017 for a detailed discussion). In PNM, where all triples have $T = 3/2$, these 3*N* forces usually vanish and it can be shown that at N^{2}LO only the long-range 3*N* TPE interaction contributes (see, for instance, Hebeler & Schwenk 2010), while shorter-range contributions to PNM only appear at higher-order in the chiral expansion. In our case, however, contributions to PNM from short-range N^{2}LO 3*N* interactions arise as artifacts from using local regulators. Local forces in coordinate space are essential for their incorporation in AFDMC but introduce regulator artifacts; see Huth et al. (2017) for a detailed discussion in the NN sector. In the case of three-nucleon forces, these regulator artifacts appear in form of shorter-range 3*N* interactions mixed into triples with $S = 3/2$ or $T = 3/2$, e.g., triples containing three neutrons. We include these additional contributions, which we denote as N^{2}LO TPE $+V_{E,\mathbb{1}}$ and N^{2}LO TPE$+V_{E,\tau}$, to provide even more conservative uncertainty estimates.

It is interesting to analyze the predictions for the energy per particle and the pressure of PNM at $2n_0$. From Table 1 and comparing the LO, NLO, and N^{2}LO TPE-only predictions, the pattern of convergence for the energy per particle is quite reasonable, with clear signs of an order-by-order improvement. For the pressure, the NLO contribution is larger than expected from naive power counting arguments. A plausible resolution of this discrepancy could be important contributions due to the Δ isobar, which are only included at N^{2}LO in Δ-less chiral EFT. We note, however, that the more conservative error estimates in brackets assuage the tension somewhat. The improvement in predictions for the pressure at $2n_0$ from NLO to N^{2}LO (TPE-only), on the other hand, is consistent with EFT expectations. The situation for the TPE$+V_{E,\mathbb{1}}$ and TPE$+V_{E,\tau}$ interactions is less satisfactory. For the TPE$+V_{E,\mathbb{1}}$ interaction, the predicted pressure at N^{2}LO has some overlap with the error band at NLO, while for the TPE$+V_{E,\tau}$ interaction the overlap is negligible. It is particularly troubling that the TPE$+V_{E,\tau}$ interaction predicts negative pressures at $2n_0$.

As argued earlier, these shorter-range contributions are an artifact of using local regulators. The large attractive contribution of the TPE$+V_{E,\tau}$ interaction is unphysical and should be discarded for the following reasons: (i) the full N^{2}LO 3N contributions in momentum-space calculations by Hebeler & Schwenk (2010), Tews et al. (2013), Hagen et al. (2014), Sammarruca et al. (2015), Wlazowski et al. (2014), and Drischler et al. (2016) are all found to be repulsive in PNM; (ii) the inclusion of N^{3}LO 3*N* contributions does not change the repulsive nature of 3*N* forces in PNM, see Krüger et al. (2013) and Drischler et al. (2016); and (iii) local regulators lead to less repulsion from the 3*N* TPE compared to typically used nonlocal regulators (Tews et al. 2016; Dyhdalo et al. 2016). For these reasons, we will ignore the N^{2}LO TPE$+V_{E,\tau}$ interaction in the following but include the TPE$+V_{E,\mathbb{1}}$ interaction to investigate more repulsive short-range 3*N* forces.

It is worth noting that the pressure predicted by the phenomenological AV8′+UIX interaction at $2n_0$ is significantly larger than the N^{2}LO (TPE-only) prediction. Even the inclusion of additional repulsion through the N^{2}LO TPE$+V_{E\mathbb{1}}$ interaction does not alleviate this discrepancy. With some reserve, we propose that our calculations with the N^{2}LO TPE $+V_{E,\mathbb{1}}$ interaction provide an upper limit to the pressure. Calculations with local chiral interactions suggest that $P(2n_0) < 20\,\mathrm{MeV\,fm^{-3}}$ in PNM, see Table 1.

In the following, we use the PNM results from the chiral N^{2}LO TPE-only and TPE+ $V_{E,\mathbb{1}}$ interactions up to a transition density n_{tr}, which we vary in the range of 1–2n_0. Although the

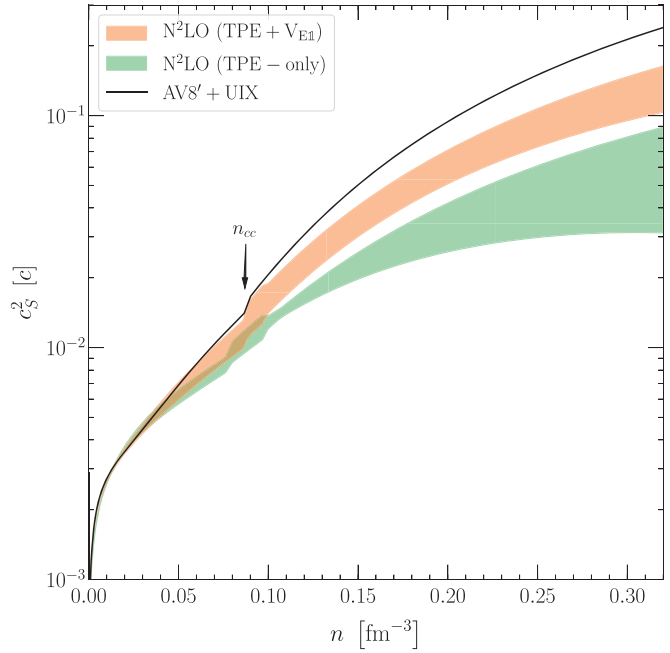

Figure 3. Speed of sound as a function of density for NS matter based on the local chiral N^{2}LO TPE-only (green lower band) and TPE+$V_{E,\mathbf{1}}$ (red higher band) interactions of Lynn et al. (2016) and the AV8′+UIX interaction (black line) for comparison. The arrow indicates the region of the crust-core transition.

uncertainties are sizable at $2n_0$, we shall find that PNM calculations still provide useful constraints. The phenomenological AV8′+UIX interaction will also be analyzed in the same density interval for comparison. Even though the expansion parameter $\simeq k_F/\Lambda_B$ only increases by about 25% when the density is increased from n_0 to $2n_0$, we have chosen $2n_0$ as an upper limit to the validity of nuclear Hamiltonians for the following reasons. First, the previous discussion of uncertainties and the order-by-order convergence of the energy per particle and pressure in neutron matter has shown that while the convergence for the energies is consistent with EFT expectations, the situation is less satisfactory for the pressure at $2n_0$. Second, the accuracy of chiral nuclear interactions in describing typical momenta in nuclei and nucleon–nucleon scattering data decreases with increasing density. Third, at higher densities, additional degrees of freedom, e.g., hyperonic dof, might appear (e.g., Ambartsumyan & Saakyan 1960; Glendenning 1982; Lonardoni et al. 2015; Gal et al. 2016). Fourth, at densities above $2n_0$, typical momenta in neutron matter are comparable to the cutoff scales employed in the calculation, which further increases the size of regulator artifacts. Based on these reasons, we believe that $2n_0$ is a reasonable upper bound for calculations with the local chiral Hamiltonians that we employ here.

2.2. The EOS of NS Matter

Matter in NS is in β—equilibrium, and at the relevant densities a small fraction of protons will be present. The proton fraction, denoted by x, increases with density but remains small and $x \lesssim 10\%$ even at $2n_0$. Although the proton contribution to the EOS can be expected to be small compared to the intrinsic uncertainty associated with the nuclear Hamiltonian discussed earlier, we shall extend the PNM results to finite proton fraction. To achieve this, we use the parameterization introduced by Hebeler et al. (2013), given by

$$\frac{E^{\rm nuc}}{A}(n,x) = T_0\Bigg[\frac{3}{5}(x^{\frac{5}{3}}+(1-x)^{\frac{5}{3}})\left(\frac{2n}{n_0}\right)^{\frac{2}{3}} - [(2\alpha-4\alpha_L)x(1-x)+\alpha_L]\cdot\frac{n}{n_0} + [(2\eta-4\eta_L)x(1-x)+\eta_L]\cdot\left(\frac{n}{n_0}\right)^{\gamma}\Bigg], \quad (4)$$

where $T_0 = (3\pi^2 n_0/2)^{2/3}\hbar^2/(2m_N)$ is the Fermi energy of noninteracting symmetric nuclear matter at saturation density, $x = n_p/n$ is the proton fraction (n_p is the proton density), and α, α_L, η, η_L, and γ are parameters that are fit to the neutron-matter results and the saturation point of symmetric nuclear matter, $\frac{E^{\rm nuc}}{A}(n_0, 0.5) = -16$ MeV, and $P^{\rm nuc}(n_0, 0.5) = 0$. The saturation point determines α and η, while the parameters α_L, η_L, and γ are determined by the PNM results. This parameterization provides a faithful reproduction of the PNM results obtained using AFDMC for densities up to $2n_0$, and has also been shown to provide a good representation of results for asymmetric nuclear matter obtained in many-body perturbation theory (Drischler et al. 2014).

Using the parameterization in Equation (4), we follow Tews (2017) to construct a consistent crust model up to the crust-core transition density, $n_{cc} \approx n_0/2$. For densities between n_{cc} and the chosen transition density $n_{\rm tr}$, we extend the PNM results to β equilibrium. From this procedure, the neutron-star equation of state $P(\epsilon)$ and the speed of sound $c_S^2(n)$ are determined. In Figure 3, we show the speed of sound in NS matter up to two times nuclear saturation density for the chiral N^{2}LO TPE-only (green band), N^{2}LO TPE+$V_{E,\mathbf{1}}$ (red band), and AV8′+UIX (black line) interactions.

3. Speed-of-sound Extension to Higher Densities

To obtain the mass–radius relation of NSs we need to extend our EOS of NS matter to higher densities. A common approach is to use a polytropic extension (see, e.g., Hebeler et al. 2013; Kurkela et al. 2014, and Raithel et al. 2016 for more details). In such an approach, the higher-density EOS is parameterized by a set of piecewise polytropes, that are matched to the microscopic calculations. The polytropic indices and the transition densities between the individual segments are then varied to sample many possible EOS curves. This approach is rather general but it leads to discontinuities in the speed of sound.

In this work, we shall restrict our analysis to scenarios for which the speed of sound is continuous for densities encountered inside NS, allowing us to directly parameterize the speed of sound and use it to construct the EOS. Although this may be less general than EOSs constructed from piecewise polytropes, our choice is motivated by the following observation. Our calculations of the nuclear EOS up to $2n_0$ show that it is relatively soft with a rather small speed of sound. To obtain a maximum NS mass $M_{\rm max} > 2\ M_\odot$, the EOS at higher density needs to stiffen significantly. This disfavors strong first-order phase transitions inside NS above $2n_0$, and models of high-density matter where new Fermionic or bosonic degrees of freedom appear suddenly to produce discontinuities in the energy density (note that the pressure is continuous and

monotonically increasing toward the center of NS due to hydrostatic equilibrium; Alford et al. 2013). Without such phase transitions, it is more natural to expect that the evolution of the speed of sound in the NS core will be continuous. In the following, we shall connect the speed of sound in neutron matter at densities up to $1-2n_0$ shown in Figure 3, to the speed of sound expected in deconfined quark matter at very high density (Kurkela et al. 2010) using two parameterizations, that we will discuss in Sections 3.1 and 3.2.

We stress that sampling the speed of sound is a complimentary approach to using a set of piecewise polytropes. In fact, choosing a set of piecewise polytropes is completely equivalent to choosing piecewise segments for the speed of sound that have a specific functional form and are connected by phase transitions, e.g., three segments with three such phase transitions in the case of Hebeler et al. (2013). Sampling the speed of sound allows us to easily control the number of phase transitions as well as their characteristics and to extract meaningful information on its density behavior, e.g., the maximum speed of sound inside an NS and its peak position. It is also straightforward to include additional information on the speed of sound, e.g., bounds on c_S. In Section 3.1, we will analyze the impact of such a bound.

3.1. Extension with the Conformal Limit

In this scenario $c_S^2 < 1/3$ at all densities, and we extend the speed of sound to densities above those described by the nuclear EOS using a simple three-parameter curve,

$$c_S^2 = \frac{1}{3} - c_1 \exp\left[-\frac{(n-c_2)^2}{n_{\rm BL}^2}\right], \tag{5}$$

where two of the parameters, c_1 and c_2, are fit to the speed of sound and its derivative at $n_{\rm tr}$. The remaining parameter, $n_{\rm BL}$, controls the width of the curve and presents a density interval in which the speed of sound changes considerably. The smaller this parameter, the stronger the change of the speed of sound with density. By varying this remaining parameter, we can easily control the slope of the speed of sound after the transition density, see Figure 4. The choice of an exponential function may seem ad hoc at this stage, but will be well motivated shortly when we find that to obtain $2\,M_\odot$ NSs, c_S must increase rapidly over a narrow interval $n_{\rm BL} \lesssim n_0$.

From Equation (5), we can construct the EOS using the following procedure. Starting at $n_{\rm tr}$, where $\epsilon(n_{\rm tr})$, $p(n_{\rm tr})$, and $\epsilon'(n_{\rm tr})$ are known, we take successive small steps Δn in density,

$$n_{i+1} = n_i + \Delta n \tag{6}$$

$$\epsilon_{i+1} = \epsilon_i + \Delta\epsilon = \epsilon_i + \Delta n \cdot \left(\frac{\epsilon_i + p_i}{n_i}\right) \tag{7}$$

$$p_{i+1} = p_i + c_S^2(n_i)\cdot\Delta\epsilon, \tag{8}$$

to iteratively obtain the high-density EOS, where the index $i=0$ defines the transition density $n_{\rm tr}$. Note, in the second line we have used the thermodynamic relation $p = n\partial\epsilon/\partial n - \epsilon$ valid at zero temperature. We then use the resulting equation of state to solve the Tolman–Oppenheimer–Volkoff (TOV) equations, and to obtain the mass–radius relation for NS.

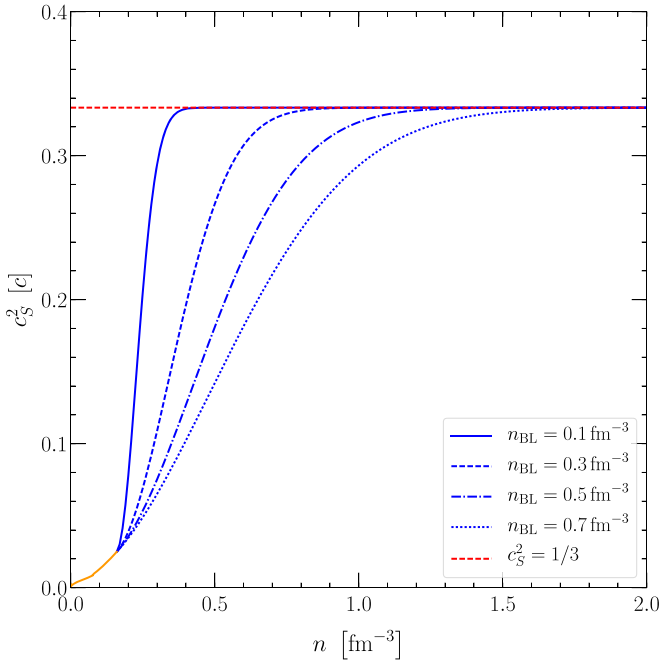

Figure 4. Extension for c_S^2 as a function of density n as defined in Equation (5). The orange line represents the constraint from the TPE-only EOS (up to $n_{\rm tr} = 0.16$ fm^{-3}), while the blue lines are extensions for several widths ($n_{\rm BL} = 0.1, 0.3, 0.5, 0.7$ fm^{-3} from left to right). The red dashed line indicates the conformal limit.

In Figure 5, we show the maximum NS mass as a function of the baseline width $n_{\rm BL}$ of Equation (5) (describing the slope) for two transition densities, $n_{\rm tr,1} = 1.1n_0 = 0.18\,{\rm fm}^{-3}$ and $n_{\rm tr,2} = 2n_0 = 0.32\,{\rm fm}^{-3}$, and for the nuclear interactions of Figure 3. We compare these to the current NS maximum-mass constraint of $2.01 \pm 0.04\,M_\odot$ (Antoniadis et al. 2013). Depending on the transition density and the nuclear Hamiltonian, we observe the tension between current nuclear and astrophysical constraints and the $c_S^2 < 1/3$ bound set by the conformal limit, first noted in Bedaque & Steiner (2015; see also Moustakidis et al. 2017). At the lower transition density, there is some freedom to find an EOS that satisfies both the conformal bound and the maximum-mass constraint. However, the inferred value of $n_{\rm BL}$ is small, indicating that c_S must increase much more rapidly in the density interval $n_0 - 2n_0$ than would be compatible with EFT predictions. For $n_{\rm tr} = 2n_0$, chiral EFT, even with the repulsion beyond the TPE-only interaction, is unable to support the $2.01 \pm 0.04\,M_\odot$ NS if the conformal bound is observed. The stiffest EOS predicted by the phenomenological Hamiltonian AV8′+UIX (black line) barely satisfies both bounds in that case.

In the left panel of Figure 6, we show the evolution of c_S^2 for the largest values of $n_{\rm BL}$ compatible with a two-solar-mass NS for several transition densities and for the softest and stiffest nuclear interaction under investigation (without uncertainty bands for clarity). In the right panel, we show this maximal width as a function of $n_{\rm tr}$. We find that for the chiral N^{2}LO TPE-only interaction there is no curve that satisfies both the speed-of-sound and the NS-mass bounds for transition densities larger than ≈ 0.25 fm^{-3}. For the phenomenological nuclear Hamiltonian, the situation is only slightly different. We find that for low transition densities a moderate slope of the speed of sound is sufficient to reproduce a two-solar-mass NS. With

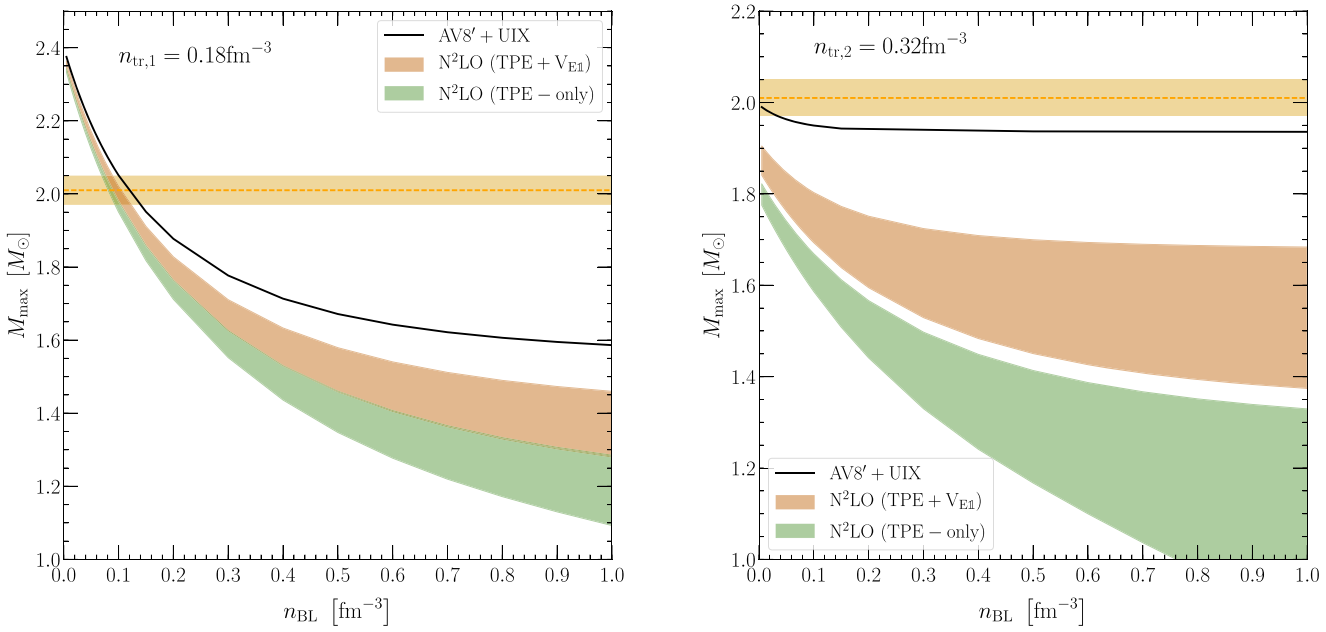

Figure 5. Maximum mass $M_{\rm max}$ as a function of baseline width $n_{\rm BL}$ of Equation (5) for the chiral N^{2}LO interactions (red and green bands), and the AV8′+UIX interaction (black line) for two transition densities, $n_{\rm tr,1} = 0.18$ fm^{-3} and $n_{\rm tr,2} = 0.32$ fm^{-3}. We also indicate the highest observed NS mass with its uncertainty (orange band).

increasing transition density, again, the speed of sound has to increase on a smaller density interval to fulfill the mass constraint. Above transition densities of $\approx 0.3\,{\rm fm}^{-3}$, we find strong tension between both bounds.

To summarize, since AFDMC predictions for the EOS using EFT interactions are very reliable, and order-by-order convergence at these densities was observed, we argue that our results suggest that either QCD violates the conformal bound, or a chiral EFT-based description breaks down at densities below $2n_0$ due to new physical effects.

3.2. Extension without Conformal Limit

We shall now allow the speed of sound to exceed the conformal limit of $1/\sqrt{3}$ at the densities encountered in the NS core and only require that $c_S < 1$. We model its evolution with density in a minimalist approach constrained by knowledge of its behavior at low and high density by adding a skewed Gaussian to the form defined in Equation (5),

$$c_S^2 = \frac{1}{3} - c_1 \exp\left[-\frac{(n-c_2)^2}{n_{\rm BL}^2}\right] + h_{\rm P} \exp\left[-\frac{(n-n_{\rm P})^2}{w_{\rm P}^2}\right]\left(1 + {\rm erf}\left[s_{\rm P}\frac{(n-n_{\rm P})}{w_{\rm P}}\right]\right), \quad (9)$$

where the peak is described by its height $h_{\rm P}$, position $n_{\rm P}$, width $w_{\rm P}$, and the shape or skewness parameter $s_{\rm P}$. The coefficients c_1 and c_2 are again adjusted to the microscopic calculations up to the transition density $n_{\rm tr}$ to make sure that the speed of sound and its derivative are continuous. By varying the remaining parameters, we can model many possible curves for the speed of sound. In Figure 7, we show four such parameterizations where we also indicate the maximal central density reached for each EOS. As one can see, this approach is very versatile and can produce very different shapes for the speed of sound, some of which resemble the result by Paeng & Rho (2016).

The chosen form in Equation (9) allows c_S to be a nonmonotonic function of density. The peak at intermediate density can be interpreted as describing a crossover transition that may be realized inside NSs. However, the high-density behavior, where $c_S^2 \approx 1/3$, is realized at densities well beyond those accessed in NSs. While this functional form is rather simple and has only five parameters, it is comparable in complexity to a polytropic extension with three polytropic segments, and can be easily extended. We have also tested different functional forms for the speed of sound and found our results to be robust: the average radius for a typical $1.4\,M_\odot$ NS varied only on the percent level when different functional forms were chosen.

We sample values for the baseline width and the four peak parameters that determine c_S to construct the high-density EOS. We use the full EOS and solve the TOV equations to obtain NS mass–radius curves and the NS maximum mass; when this is found to be greater than the $2.01\,M_\odot$ mass constraint, we accept the parameter set, and reject it otherwise. We sample the five parameters from uniform distributions within the following ranges: $n_{\rm BL}$ between 0.01 and $3.0\,{\rm fm}^{-3}$, $h_{\rm P}$ between 0.0 and 0.9, $w_{\rm P}$ between 0.1 and $5.0\,{\rm fm}^{-3}$, $n_{\rm P}$ between $(n_{\rm tr} + 0.08) - 5.0\,{\rm fm}^{-3}$, and $s_{\rm P}$ between $(-50) - 50$, and enforce that $0 \leqslant c_S^2 \leqslant 1$.

For the chiral interactions, we additionally sample from the uncertainty bands for c_S by randomly choosing a factor $f^{\rm err}$ between -1 and 1, that linearly interpolates between the lower and upper bounds of the uncertainty band,

$$c_S(n) = c_S^{\rm N^2LO}(n) + f^{\rm err}\,\Delta c_S^{\rm EKM}(n), \quad (10)$$

where $c_S^{\rm N^2LO}(n)$ is the chiral result at N^{2}LO and $\Delta c_S^{\rm EKM}(n)$ is its uncertainty.

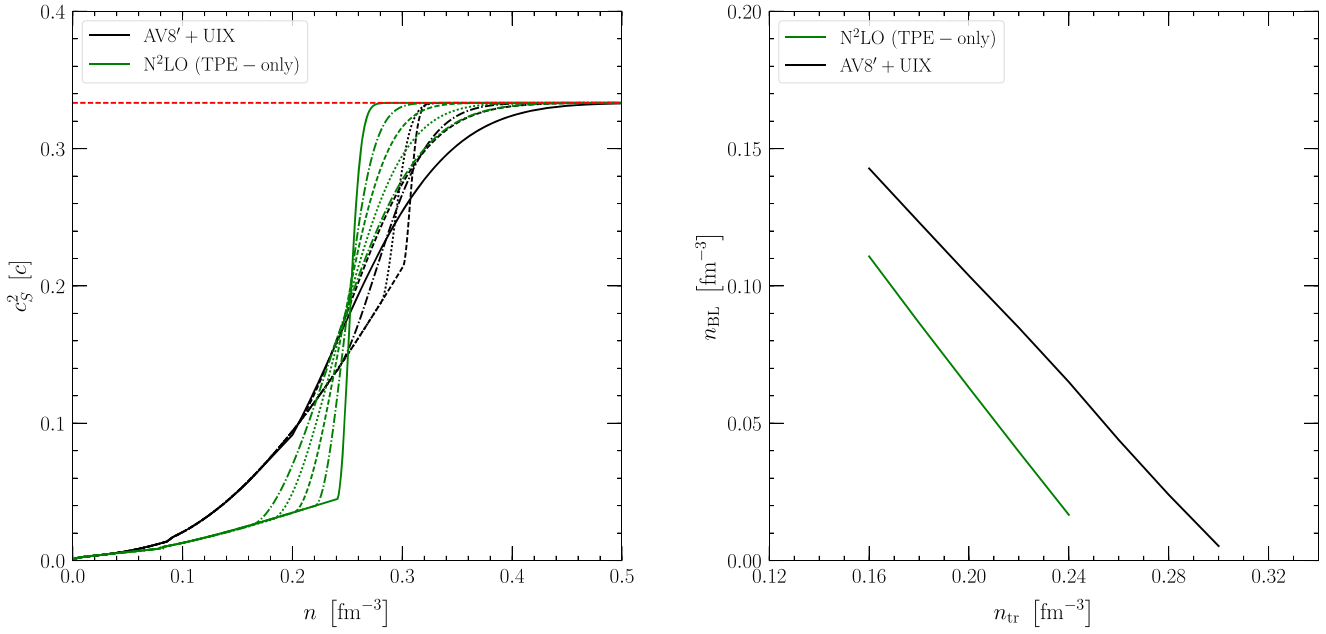

Figure 6. Left panel: c_S^2 as a function of density for several transition densities and two nuclear Hamiltonians. For each transition density and Hamiltonian, we show the curve for the maximal $n_{\rm BL}$ that still supports a two-solar-mass NS. Right panel: the maximal $n_{\rm BL}$ that is sufficient to support a two-solar-mass NS as a function of transition density for the same Hamiltonians.

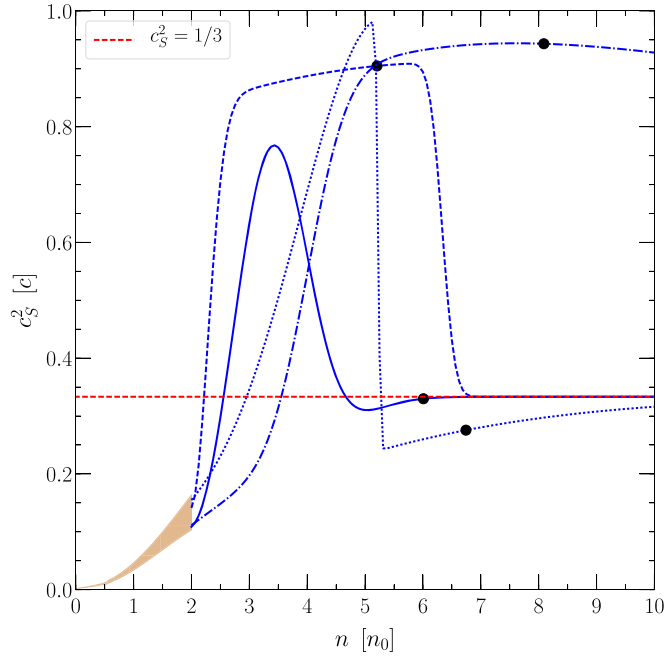

Figure 7. Four examples for the extension of $c_S^2(n)$ as defined in Equation (9) (without conformal limit) for $n_{\rm tr,2}$ and the chiral TPE+$V_{E,1}$ interaction. Black dots indicate the maximal central densities reached inside NSs for the corresponding EOSs and the red dashed line indicates the conformal limit.

As stated before, we analyze the results for two different transition densities and generate a few thousand accepted parameter sets for each transition density. We show histograms for the resulting speed of sound, the mass–radius relation, and the EOS in Figures 8 and 9 for both transition densities. For the mass–radius histograms, we also show the average radius for each mass as well as 68% confidence intervals.

We find that the speed of sound increases rapidly in a small density range above $n_{\rm tr}$. This increase is more drastic for softer nuclear interactions. For stiffer interactions, c_S increases slowly and peaks at higher densities. In all cases, for a large fraction of parameterizations, the speed of sound increases to values around $c_S \approx 0.9$. For the smaller transition density, there exist parameterizations that observe the conformal limit at all densities, while for the higher transition density all parameterizations violate this bound, consistent with our previous findings.

For the mass–radius relation, we find a rather broad radius distribution at lower transition densities that narrows with increasing transition density. This highlights the fact that PNM calculations at densities $\sim 2n_0$ provide valuable information despite sizable uncertainties. We highlight this fact in Figure 10, where we show the radius of a typical 1.4 $M_\odot$ NS as a function of $n_{\rm tr}$ for the chiral EFT interactions. At $n_{\rm tr,1}$, we find a radius range of 9.4–14.0 km (10.0–14.1 km) with a 68% confidence interval of 12.0 ± 1.0 km (12.3 ± 0.9 km) for the TPE-only (TPE+$V_{E,1}$) interaction. This range reduces to 9.4–11.8 km (10.2–12.3 km) with a 68% confidence interval of 10.7 ± 0.5 km ($11.5^{+0.3}_{-0.4}$ km) for $n_{\rm tr,2}$.

For the phenomenological interaction, the mass–radius relation is much narrower than for the chiral interactions because the EOS is much stiffer and uncertainties associated with the interaction are unknown. For a typical NS, we find a radius range of 11.4–14.3 km with a 68% confidence interval of $12.7^{+0.7}_{-0.6}$ for $n_{\rm tr,1}$ and a very narrow range of 12.8–12.9 km for $n_{\rm tr,2}$.

In all histograms, we compare our findings to the corresponding envelopes of Hebeler et al. (2013) for a polytropic expansion with three polytropes and find very good agreement for all interaction models. This suggests that our extension is general enough to capture similar effects as the polytropic extension. Our results are also consistent with other radius constraints using EOSs obtained with the AFDMC method (Steiner & Gandolfi 2012; Steiner et al. 2015).

In Table 2, we show the maximum masses and the maximal central densities for all interactions and both transition densities. The upper limit for the maximum mass strongly

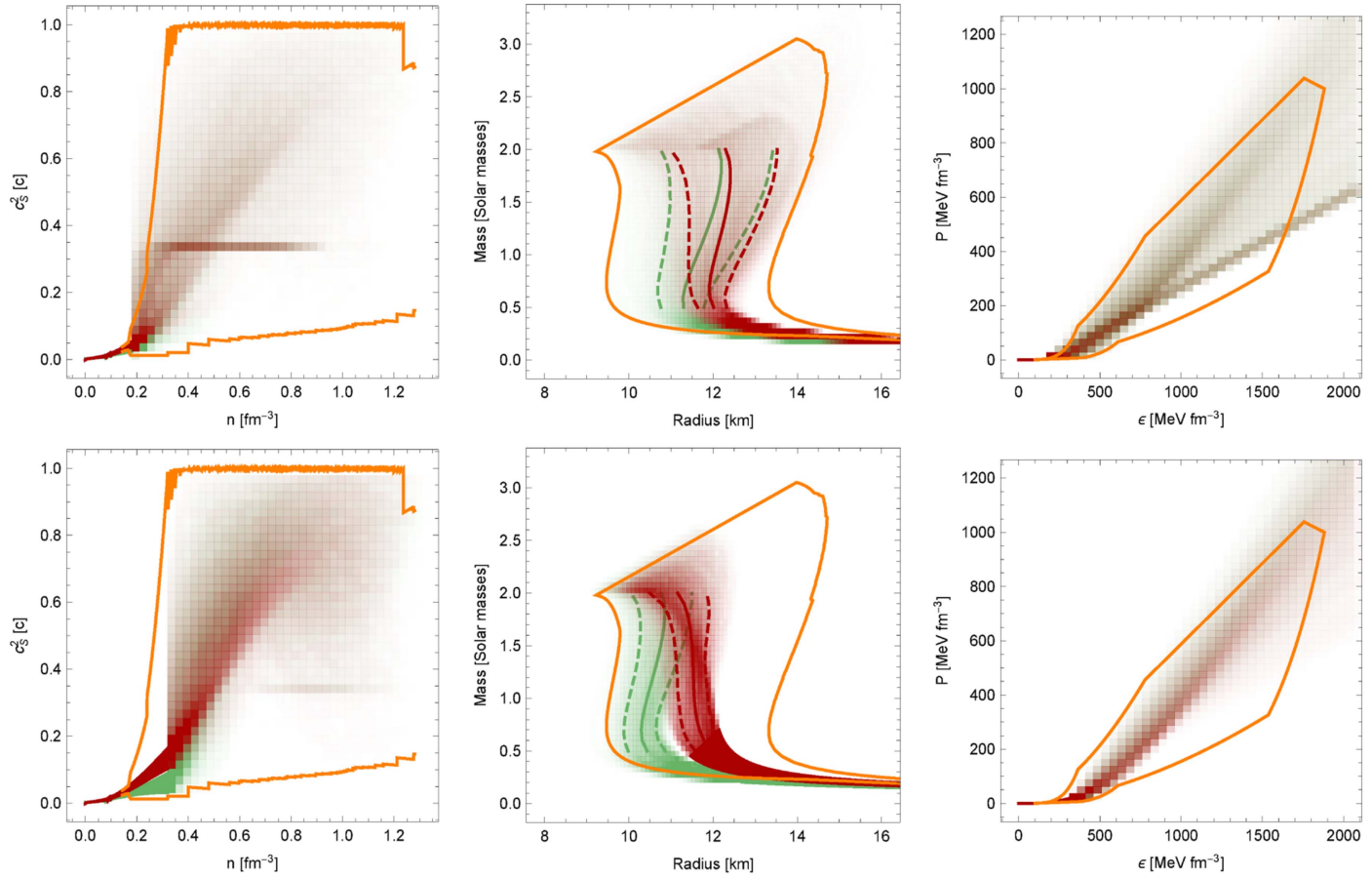

Figure 8. Histograms for $c_S^2(n)$, the mass–radius relation, and the EOS for all the accepted parameter sets for the local chiral N^{2}LO interactions of Figure 3 and $n_{tr,1}$ (upper panels) and $n_{tr,2}$ (lower panels). For the $c_S^2(n)$ histogram, we terminate each parameterization at its maximal central density. The orange lines are the corresponding contours for the polytropic expansion of Hebeler et al. (2013). For the mass–radius curve, we also show the average radius for each mass (solid line) as well as 68% confidence intervals (dashed lines).

depends on the chosen transition density but not on the interaction. For the smaller transition density, the highest achievable maximum mass is $\approx 3.6\,M_\odot$, independent of the interaction. For the higher transition density, the highest achievable maximum mass is $\approx 2.8\,M_\odot$ for all interactions. The maximal central density reached inside the NS, $n_{c,\max}$, that is, the central density in the maximum-mass NS, ranges between 2.7 and $8.9 n_0$ for the lower transition density, and 4.4–$9.3 n_0$ for the larger transition density.

Kurkela et al. (2014), Fraga et al. (2016), and Annala et al. (2018) discussed the possibility of additionally constraining the EOS with information from pQCD at very high densities. Their calculation constrains the pressure at $\epsilon \approx 15000\,\mathrm{MeV\,fm^{-3}}$ to lie in the range of $p \approx 2600$–$4000\,\mathrm{MeV\,fm^{-3}}$. However, we find that the highest pressure inside any stable NS $p_{\max} \approx 1570\,\mathrm{MeV\,fm^{-3}}$ is significantly smaller. Since we cannot infer the EOS at densities above the maximum central density from NS observations, it is always possible to find curves for the speed of sound with $0 \leqslant c_S^2 \leqslant 1$ that connect our models at the maximal central density with the pQCD constraint.

3.3. Parameter Correlations

In the following, we want to discuss correlations between $n_{c,\max}$ and $M_{\max}$, and $c^2_{S,\max}$ and $M_{\max}$. We show histograms for these correlations in Figure 11 for the chiral interactions and $n_{\mathrm{tr},2}$, but our observations do not change significantly for the other interactions or transition densities.

The correlation between $n_{c,\max}$ and $M_{\max}$ indicates, as expected, that the central densities of the heaviest NSs decrease with maximum mass. The same is true for the uncertainties of the central density, which also decrease with maximum mass. Furthermore, these central densities are well below the upper limit established by Lattimer & Prakash (2005).

For the correlation between $M_{\max}$ and $c^2_{S,\max}$, we find that the highest masses can only be reached for the stiffest EOS, i.e., EOS with highest possible $c^2_{S,\max} = 1$. Furthermore, for every maximum mass there is a minimum for $c^2_{S,\max}$ that is needed to support this mass. It follows that a maximum mass observation will give a lower bound to the maximum speed of sound. For the current maximum mass constraint, $M_{\max} = 2\,M_\odot$, $c^2_{S,\max} \geqslant 0.4$ for $n_{\mathrm{tr},2}$, which is in excellent agreement with the findings of Alsing et al. (2018). An observation of a $2.4\,M_\odot$ NS would require $c^2_{S,\max} \geqslant 0.6$.

4. Smallest Possible NS Radius

In this section, we investigate the smallest possible NS radius consistent with ab initio calculations of neutron matter and the observation of $2\,M_\odot$ NSs. This radius is found for the softest

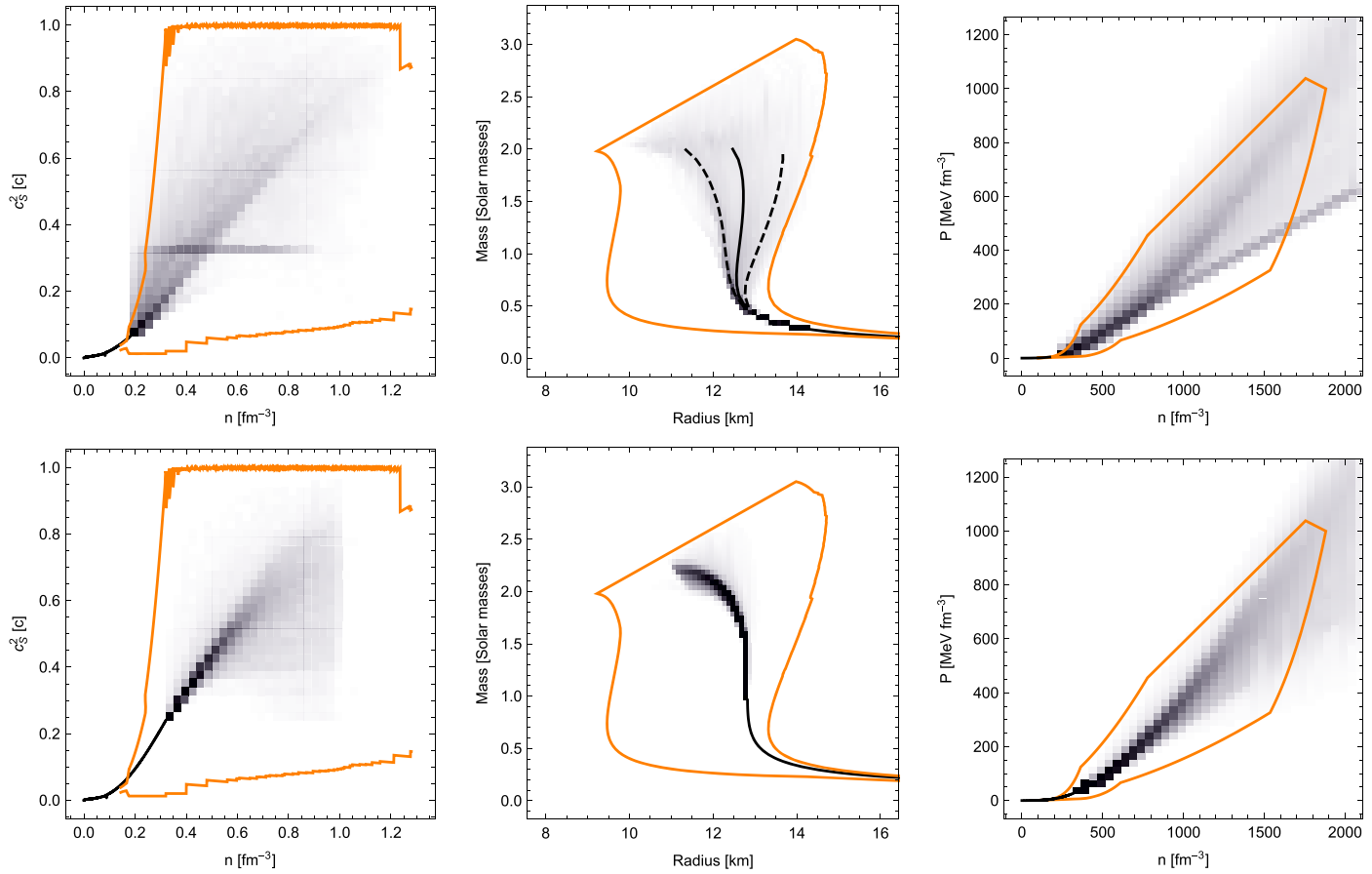

Figure 9. Same as Figure 8 but for the AV8′+UIX interaction (black line in Figure 3).

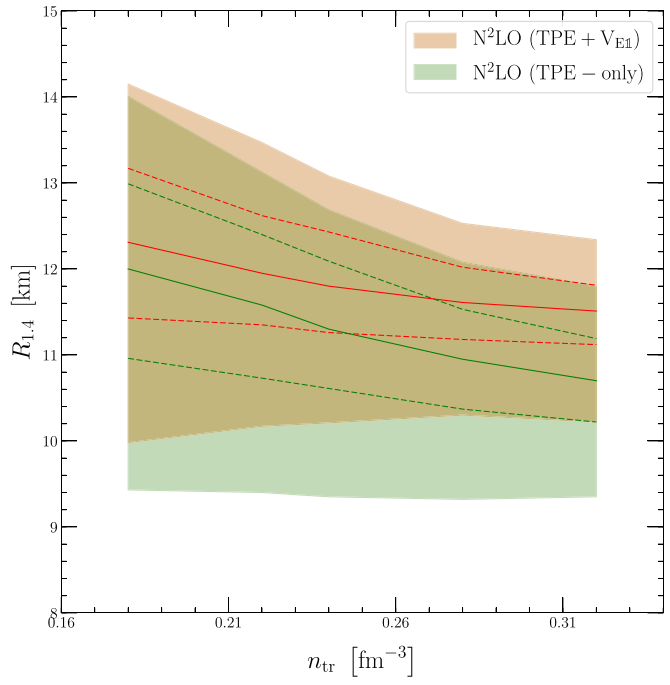

Figure 10. Radius of a 1.4 $M_\odot$ NS as a function of transition density for the chiral models. We show the total range of models (colored bands) as well as the mean (solid lines) with 68% intervals (dashed lines).

possible low-density EOS combined with the stiffest possible high-density EOS consistent with these constraints (Koranda et al. 1997).

Table 2
Maximal NS Mass and Maximal Central Densities

n_{tr} (fm^{-3})	Interaction	M_{max} ($M_\odot$)	$n_{c,max}$ (n_0)
0.18	TPE-only	2.01–3.63	2.8–8.6
	TPE+$V_{E,1}$	2.01–3.66	2.7–8.9
	AV8′+UIX	2.01–3.57	2.9–8.4
0.32	TPE-only	2.01–2.79	4.6–8.7
	TPE+$V_{E,1}$	2.01–2.81	4.5–9.3
	AV8′+UIX	2.01–2.84	4.4–8.9

Note. Maximal NS mass and maximal central densities for all interactions and both transition densities.

We again assume that ab initio neutron-matter calculations are valid up to a transition density n_1, which is at least nuclear saturation density. We choose the softest PNM EOS up to $n_1 = n_0$ to construct the lower-density part of the softest NS EOS. This EOS is given by the lower bound of the uncertainty band of the chiral N^{2}LO TPE+$V_{E,\tau}$ interaction (blue band in Figure 2). Although we did not use this interaction previously, as it leads to attractive 3N contributions and negative pressure at $1.5n_0$, it is the most conservative choice to estimate the smallest possible NS radius. We then extend this EOS to densities above n_0 in the softest way possible by setting $c_S = 0$ up to a second transition density n_2. For the EOS to be able to fulfill the second constraint, namely to reproduce a NS of a certain mass, the high-density part of the EOS has to be as stiff as possible, and above n_2, we set $c_S = 1$. This parameterization

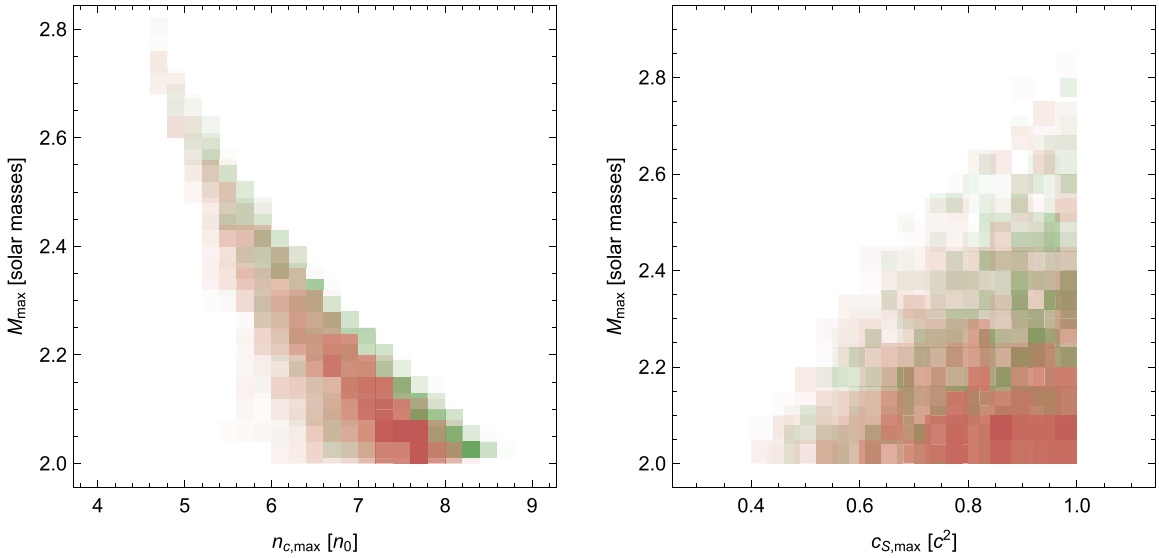

Figure 11. Histograms for the correlations between $n_{c,\max}$ and $M_{\max}$ and $c^2_{S,\max}$ and $M_{\max}$ for the chiral interactions and $n_{\mathrm{tr},2}$.

is similar to the one explored in Alford et al. (2015) and Alford & Han (2016) for $n_{\mathrm{trans}} = n_0$, and leads to the smallest radii consistent with the two constraints, because the radius is set by the low-density part of the EOS while the maximum mass is set by the high-density part. A softer high-density EOS would require a stiffer low-density EOS, which in turn would result in larger radii.

Changing the transition densities naturally affects the radius: increasing n_1 or lowering n_2 would increase the radius. The density n_2 also determines the maximum mass $M_{\max}$ that can be supported by this softest EOS. Increasing n_2 leads to decreasing maximum masses, see Figure 12. We require $M_{\max}$ to be at least consistent with the lower uncertainty bound of the heaviest observed NS, which is the case for $n_2 = 0.68\,\mathrm{fm}^{-3} = 4.25 n_0$ (solid black line). The corresponding curve represents the lowest possible neutron-star radii consistent with ab initio neutron-matter calculations and current observational constraints on NS masses. This curve implies that a typical $1.4\,M_\odot$ NS has to have a radius larger than 8.4 km.

If heavier NSs would be observed, n_2 has to decrease, which in turn leads to increasing radii; see Figure 12. For different n_2, the EOS constructed here will produce the smallest possible radius that is consistent with the corresponding $M_{\max}$. If, e.g., a $2.5\,M_\odot$ NS was observed, the radius of a typical NS would have to be larger than 10.2 km.

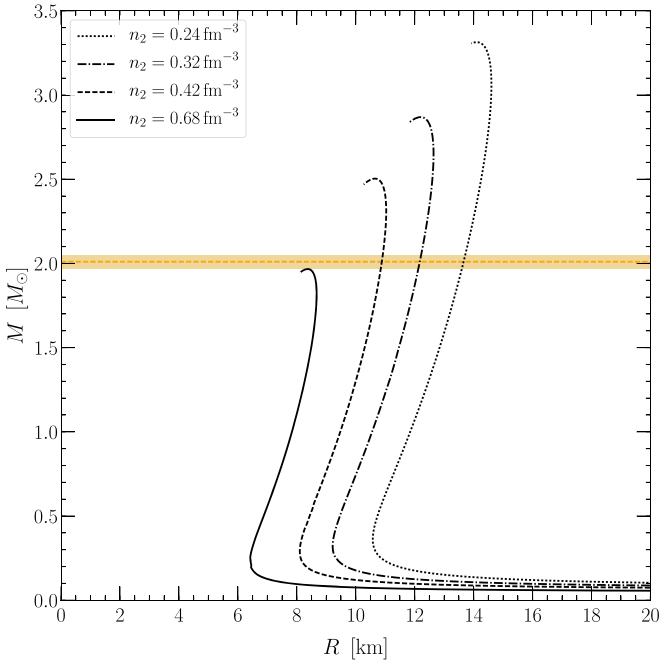

Figure 12. Mass–radius curves for the softest EOS consistent with neutron-matter calculations up to saturation density for different densities n_2. The softest EOS consistent with the observation of a $2\,M_\odot$ NS is obtained for $n_2 = 0.68\,\mathrm{fm}^{-3}$ (solid black line).

5. Impact of Additional Observations

In the following section, we investigate to what extent additional observations of NS properties, e.g., NS radii, may help to constrain the properties of nuclear interactions. We will assume in this section that we can trust nuclear interactions up to $n_{\mathrm{tr},2} = 2n_0$.

For a study of the impact of the recent NS merger observation by the Advanced LIGO collaboration (Abbott et al. 2017) using the speed-of-sound extension presented in this paper, please see Tews et al. (2018). For studies using different models for the high-density EOS constrained by chiral interactions at low densities, please see Annala et al. (2018), Most et al. (2018), and Lim & Holt (2018).

5.1. Observation of Compactness

We begin by assuming that the compactness of a NS has been observed. It was claimed by Hambaryan et al. (2017) that the compactness of the NS RX J0720.4-3125 can be inferred to be $(M/M_\odot)/(R/\mathrm{km}) = 0.105 \pm 0.002$. Margueron et al. (2018) used this information to constrain the corresponding NS mass to be $1.33 \pm 0.04\,M_\odot$ with a radius of 12.7 ± 0.3 km.

Investigating the effect of such a compactness observation, we find a rather broad range for possible neutron-star masses and radii, ranging from $M = 1.00$–$1.38\,M_\odot$ and $R = 9.8$–12.8 km. The chiral interactions favor smaller NSs, with the weight of the distribution around the point (11 km, $1.1\,M_\odot$) for the TPE-only and (12 km, $1.2\,M_\odot$) for the TPE+$V_{E,\mathbb{1}}$ interaction. The AV8′

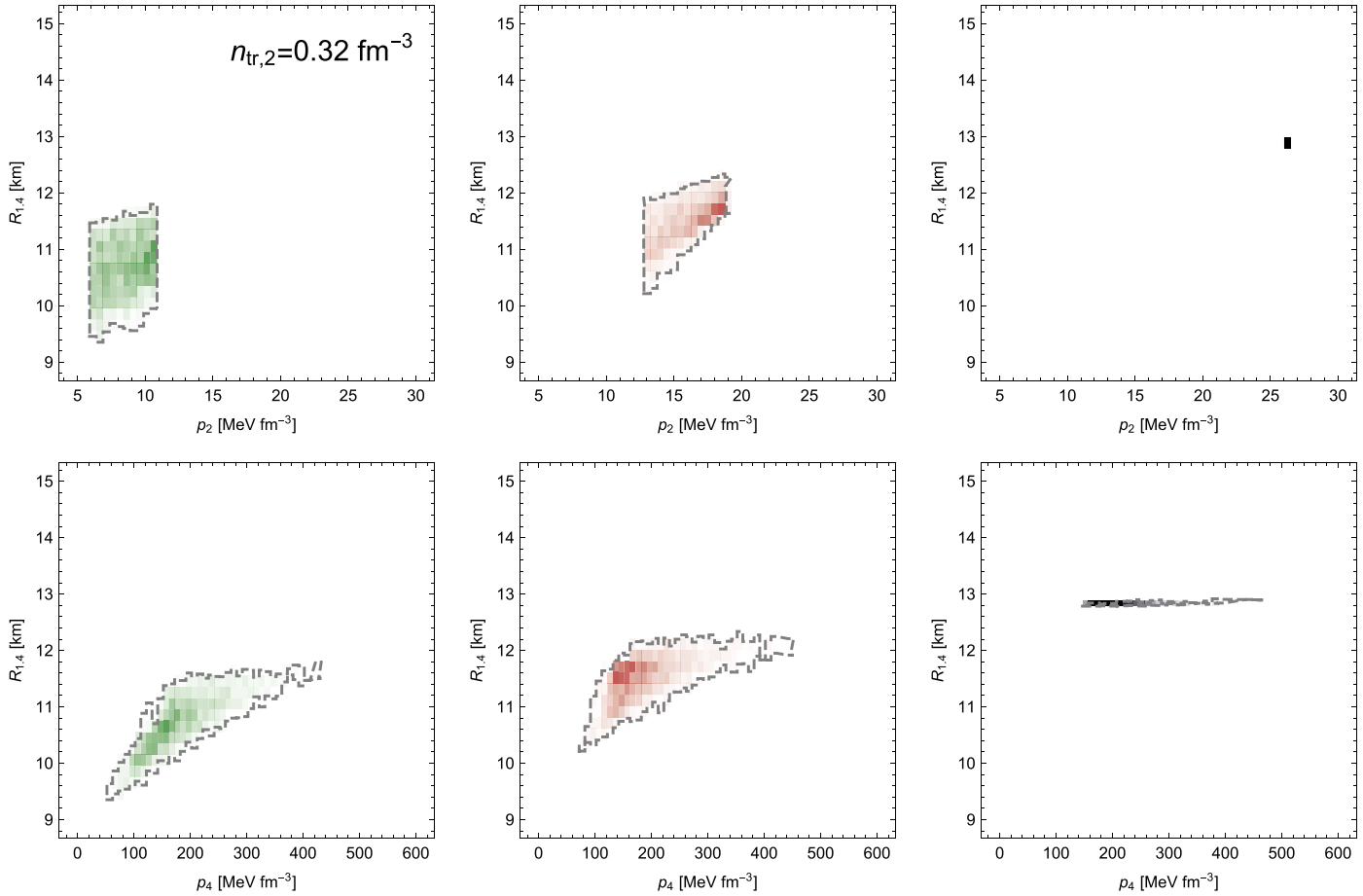

Figure 13. Histograms for the radius of a 1.4 $M_\odot$ NS, $R_{1.4}$ vs. the pressure at two times the saturation density, $p(2n_0) = p_2$ (upper panels), or the pressure at four times the saturation density, $p(4n_0) = p_4$ (lower panels), for all interactions (N^2LO TPE-only left, N^2LO TPE+$V_{E,1}$ middle, AV8′+UIX right) and $n_{tr,2}$.

+UIX interaction leads to a prediction of $M = 1.32$–$1.38\,M_\odot$ with a radius of 12.8 km, in good agreement with the prediction of Margueron et al. (2018).

The observation of the compactness alone is naturally not sufficient to further constrain the EOS. However, by observing the compactness of a star with known mass, which is equivalent to a radius measurement, additional constraints can be found. We discuss this in the next section.

5.2. Observation of the NS Radius

In the following, we investigate how possible radius measurements by the NICER mission will impact our findings for the EOS and the mass–radius curve and help to constrain the microscopic equation of state. The NICER mission, which was launched in 2017 July, is expected to measure the compactness (and, thus, radius) of at least three NSs with known masses with an accuracy of 5%–10%. Among these are (Arzoumanian et al. 2014) the NSs PSR J1023+0038 with $M = 1.71 \pm 0.16\,M_\odot$ (Deller et al. 2012), PSR J0437-4715 with $M = 1.44 \pm 0.07\,M_\odot$ (Reardon et al. 2016), and a proposal for using NICER to measure PSR J1614-2230 with a mass of $\approx 2.0\,M_\odot$ (Miller 2016).

We show histograms for the radius of a typical 1.4 $M_\odot$ NS, $R_{1.4}$, versus the pressure at two times the nuclear saturation density, $p(2n_0) = p_2$, and the pressure at four times the nuclear saturation density, $p(4n_0) = p_4$ in Figure 13, for all interactions and $n_{tr,2}$. All interactions predict different p_2, as expected, but overlapping distributions for p_4. The chiral interactions predict similar radii around 10–12 km, and the AV8′+UIX interaction predicts a higher radius of $R_{1.4} \approx 12.8$ km, which is not consistent with the chiral models; see also Figure 9.

We now assume that the radius of such a 1.4 $M_\odot$ NS is observed with an accuracy of 10%. We will focus on two extreme cases: $R_{obs} = (10 \pm 1.0)$ km, which is the lower bound on the suggested radius range of Ozel & Freire (2016), and $R_{obs} = (13 \pm 1.3)$ km, which is on the upper end of the currently accepted radius range. We show the corresponding histograms for the mass–radius relation and the speed of sound in Figure 14.

The observation of a small 10 km NS would eliminate a sizable part of the stiffer parameterizations with higher p_2 and p_4 (see also Figure 13) and would allow us to obtain additional constraints on the microscopic EOS at $n_{tr,2}$: It would (i) exclude the stiffest chiral interactions; (ii) rule out the AV8′+UIX interaction; (iii) reduce the allowed maximum mass to $\approx 2.5\,M_\odot$; and (iv) suggest that the speed of sound changes less drastically above $2n_0$ and peaks at densities of $\sim$4–5n_0 with $c_S^2 \approx 0.8 \pm 0.1c^2$.

The observation of a large 13 km NS, instead, would exclude the softest interactions. For the TPE-only interaction, for example, only a very small fraction of parameterizations would survive, and a major fraction of the uncertainty band for that interaction could be ruled out. Also, in this case, the speed of sound has to increase quickly above $2n_0$.

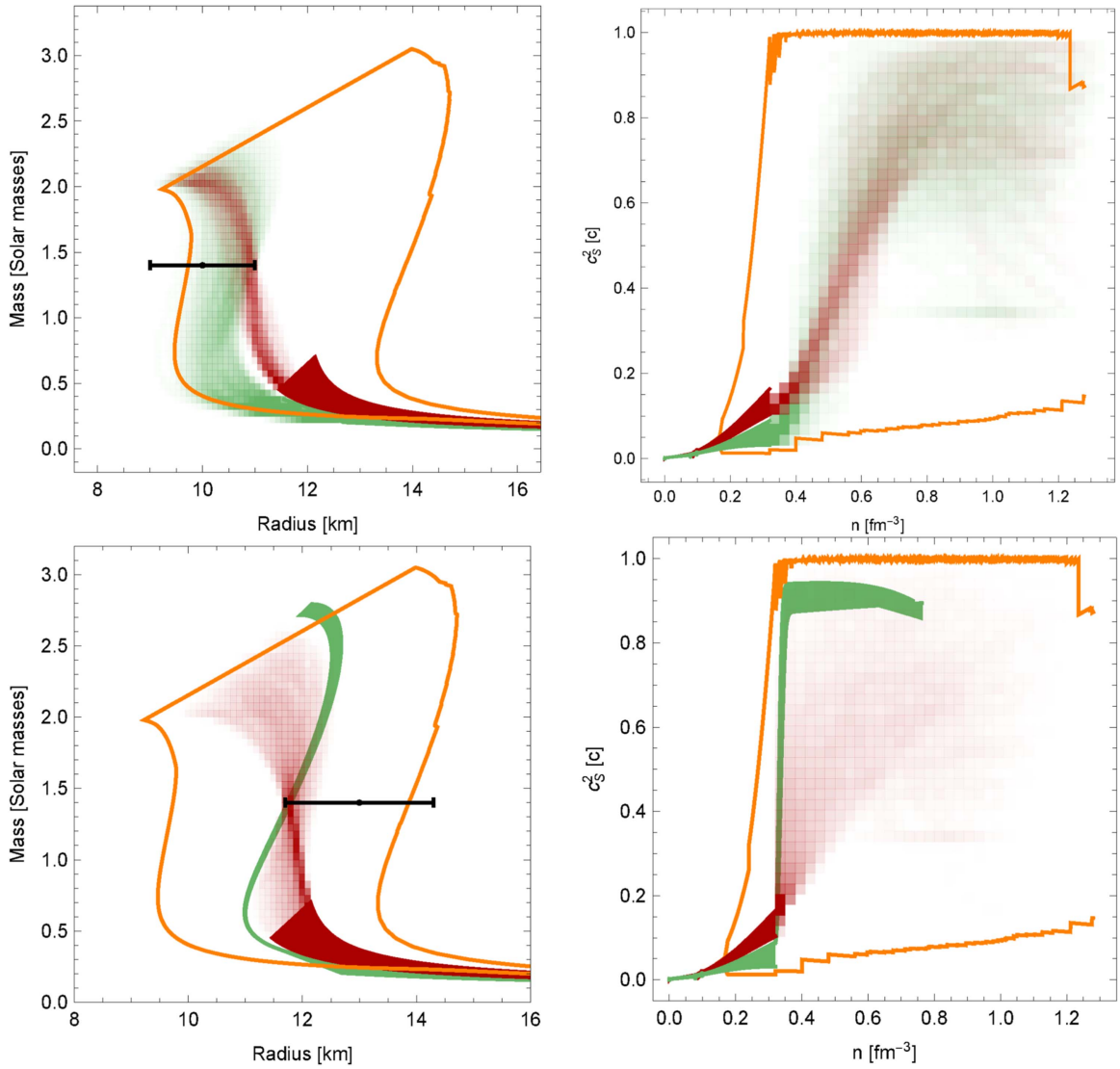

Figure 14. Upper two panels: histograms for the mass–radius relation and the speed of sound for the chiral interactions and assuming an observation of a NS with $M = 1.4\,M_\odot$ and $R = 10 \pm 1.0$ km (black point). Lower two panels: the same, assuming an observation of a NS with $M = 1.4\,M_\odot$ and $R = 13 \pm 1.3$ km.

Clearly, observations of more extreme radii and/or with smaller uncertainties would present even stronger constraints. For example, an observation of an 13 km NS with 5% uncertainty would rule out the TPE-only interaction. The prospect that NICER may achieve this precision soon with better understood systematic errors is exciting for nuclear physics and we eagerly await its results.

5.3. Observation of Two NS Radii

As we have shown in the previous section, the observation of a single NS radius might prove useful to constrain nuclear interactions, if the observed radius is either on the lower or on the upper side of the currently accepted range of 12 ± 2 km for typical $1.4\,M_\odot$ NSs. We now investigate to which extent the observation of two NS radii with 5% uncertainty for stars with known masses can be used to constrain both the EOS and nuclear interactions.

We assume that radii of a $1.4\,M_\odot$ neutron star, $R_{1.4}$, and of a $2.0\,M_\odot$ neutron star, $R_{2.0}$, have been observed, and present the pressure at twice saturation density, p_2, in Table 3 and the pressure at four times saturation density, p_4, in Table 4 for all interactions and assuming $n_{\mathrm{tr},2}$.

For $n_{\mathrm{tr},2}$, the pressure p_2 is set by the nuclear input EOS and independent of the extension. As we have shown in Section 3.2, different interactions are compatible with different ranges for $R_{1.4}$. The chiral interactions lead to $R_{1.4} \approx 10$–12 km and the AV8′+UIX interaction is only compatible with $R_{1.4} = 13\,\mathrm{km} \pm 5\%$. If, for instance, $R_{1.4} = 10\,\mathrm{km} \pm 5\%$ was observed, the AV8′+UIX interaction would be ruled out.

An additional observation of $R_{2.0}$ would permit further constraints. For instance, both chiral interactions permit $R_{1.4} = 12$ km, but only the TPE+$V_{\mathrm{E},1}$ interaction could simultaneously lead to $R_{2.0} = 10$ km. Also, the second radius observation might prove useful to constrain p_4 and the high-density equation of state. For a single radius measurement, the predicted ranges for p_4 are very large. For example, for $R_{1.4} = 12$ km, the predicted $p_4 = 107$–446 MeV fm^{-3}. A second radius measurement would allow us to clearly reduce

Table 3
Pressure at Two Times Saturation Density for Hypothetical Radius Measurements

			p_2 (MeV fm^{-3})			
				$R_{1.4}$ (km)		
			10% ± 5%	11% ± 5%	12% ± 5%	13% ± 5%
$R_{2.0}$ [km]	9% ± 5%	TPE-only	6.5–10.7			
		TPE+$V_{E,\mathbb{1}}$				
		AV8′+UIX				
	10% ± 5%	TPE-only	5.9–10.9	5.9–10.9		
		TPE+$V_{E,\mathbb{1}}$	12.8–13.6	12.8–18.1	14.7–18.9	
		AV8′+UIX				
	11% ± 5%	TPE-only	5.9–10.4	5.9–10.9	9.8–10.8	
		TPE+$V_{E,\mathbb{1}}$		12.8–18.4	12.8–18.9	
		AV8′+UIX				26.0
	12% ± 5%	TPE-only		5.9–10.9	6.1–10.9	
		TPE+$V_{E,\mathbb{1}}$		12.8–16.8	12.8–18.8	
		AV8′+UIX				26.0
	13% ± 5%	TPE-only			10.8–10.9	
		TPE+$V_{E,\mathbb{1}}$			13.1–18.8	
		AV8′+UIX				26.0

Note. Pressure at two times saturation density, p_2, for all interactions and $n_{tr,2} = 0.32$ fm^{-3}, for hypothetical simultaneous measurements of the radii of a 1.4 $M_\odot$ and a 2.0 $M_\odot$ NS, $R_{1.4}$ and $R_{2.0}$, respectively.

Table 4
Pressure at Four Times Saturation Density for Hypothetical Radius Measurements

			p_4 (MeV fm^{-3})			
				$R_{1.4}$ (km)		
			10% ± 5%	11% ± 5%	12% ± 5%	13% ± 5%
$R_{2.0}$ [km]	9% ± 5%	TPE-only	52–92			
		TPE+$V_{E,\mathbb{1}}$				
		AV8′+UIX				
	10% ± 5%	TPE-only	69–182	113–159		
		TPE+$V_{E,\mathbb{1}}$	72–112	84–152	107–141	
		AV8′+UIX				
	11% ± 5%	TPE-only	151–242	145–310	168–192	
		TPE+$V_{E,\mathbb{1}}$		122–265	117–252	
		AV8′+UIX				147–152
	12% ± 5%	TPE-only		164–428	178–428	
		TPE+$V_{E,\mathbb{1}}$		182–306	163–442	
		AV8′+UIX				148–285
	13% ± 5%	TPE-only			425–426	
		TPE+$V_{E,\mathbb{1}}$			230–446	
		AV8′+UIX				171–461

Note. Pressure at four times saturation density, p_4, for all interactions and $n_{tr,2} = 0.32$ fm^{-3}, for hypothetical simultaneous measurements of the radii of a 1.4 $M_\odot$ and a 2.0 $M_\odot$ NS, $R_{1.4}$ and $R_{2.0}$, respectively.

this range in most cases. If, for example, $R_{2.0} = 11$ km, the range for p_4 would reduce to $p_4 = 117$–252 MeV fm^{-3}.

The observation of two NS radii could be very useful to constrain both low- and high-density EOS, and will hopefully be made available by the NICER mission.

6. Summary

In this work, we used constraints on the neutron-matter EOS at low densities and general considerations for the speed of sound in NSs to investigate the structure of NSs.

We found that the conformal limit of $c_s^2 \leqslant 1/3$ is in tension with current nuclear physics constraints and observations of two-solar-mass NSs, in accordance with the findings of Bedaque & Steiner (2015). If the conformal limit was found to hold at all densities, this would imply that nuclear physics models break down below $2n_0$.

We then allowed the speed of sound to exceed the conformal limit and used general considerations about its high-density limit to parameterize the speed of sound. By using randomly sampled parameter sets and requiring the EOS to reproduce two-solar-mass NSs, we computed histograms for the speed of sound, the mass–radius relation, and the EOS for microscopic interactions from chiral EFT and the AV8′+UIX interaction. We found that the speed of sound likely exhibits a sharp increase around $2n_0$ for all interactions under consideration. We found that the upper limit on the maximum mass of NSs is 2.9–3.5 $M_\odot$, and that radii for typical 1.4 $M_\odot$ NSs range between 10 and 14 km, in agreement with the results of Hebeler et al. (2013) and Steiner et al. (2018).

We then studied the minimal possible NS radius consistent with microscopic ab initio neutron-matter calculations and NS observations, and found that a typical 1.4 $M_\odot$ NS has to have a radius larger than 8.4 km.

Finally, we studied the impact of additional observations on our models. If the compactness of a NS is observed, as suggested by Hambaryan et al. (2017), microscopic calculations allow a broad range of radii and masses for the corresponding NS. An additional mass measurement, i.e., mass and radius are known simultaneously, instead, might put tight constraints on the EOS. If the observed radius would be at the limits of the currently accepted range of 12 ± 2 km, constraints on the microscopic interactions would be possible. We have shown that the observation of two NS radii for NS with different masses will very likely permit tight constraints on nuclear interaction models and the EOS up to several times nuclear saturation density.

With the prospect of radius observations becoming available, either from the NICER mission or gravitational wave observations from NS mergers by the Advanced LIGO collaboration, an exciting era of nuclear astrophysics begins. These observations will allow us to finally pin down the EOS of NSs within the coming years.

This work was supported in part by the National Science Foundation Grant No. PHY-1430152 (JINA Center for the Evolution of the Elements), the U.S. DOE under grants Nos. DE-FG02-00ER41132 and DE-AC52-06NA25396, by the NUCLEI SciDAC program, and by the LDRD program at LANL. Computational resources have also been provided by the Jülich Supercomputing Center.

ORCID iDs

I. Tews https://orcid.org/0000-0003-2656-6355
J. Carlson https://orcid.org/0000-0002-3163-5565
S. Gandolfi https://orcid.org/0000-0002-0430-9035
S. Reddy https://orcid.org/0000-0003-3678-6933

References

Abbott, B. P., et al. LIGO Scientific and Virgo Collaborations 2017, PhRvL, 119, 161101
Alford, M. G., Burgio, G. F., Han, S., Taranto, G., & Zappalà, D. 2015, PhRvD, 92, 083002
Alford, M. G., & Han, S. 2016, EPJA, 52, 62
Alford, M. G., Han, S., & Prakash, M. 2013, PhRvD, 88, 083013
Alsing, J., Silva, H. O., & Berti, E. 2018, MNRAS, 478, 1377
Ambartsumyan, V. A., & Saakyan, G. S. 1960, SvA, 4, 187
Annala, E., Gorda, T., Kurkela, A., & Vuorinen, A. 2018, PhRvL, 120, 172703
Antoniadis, J., Freire, P. C. C., Wex, N., et al. 2013, Sci, 340, 6131
Arzoumanian, Z., Gendreau, K. C., Baker, C. L., et al. 2014, Proc. SPIE, 9144, 9144
Bedaque, P., & Steiner, A. W. 2015, PhRvL, 114, 031103
Borsanyi, S., Endrodi, G., Fodor, Z., et al. 2012, JHEP, 1208, 053
Carlson, J., Gandolfi, S., Pederiva, F., et al. 2015, RvMP, 87, 1067
Cherman, A., Cohen, T. D., & Nellore, A. 2009, PhRvD, 80, 066003
Deller, A. T., Archibald, A. M., Brisken, W. F., et al. 2012, ApJL, 756, L25
Demorest, P., Pennucci, T., Ransom, S., Roberts, M., & Hessels, J. 2010, Natur, 467, 1081
Drischler, C., Carbone, A., Hebeler, K., & Schwenk, A. 2016, PhRvC, 94, 054307
Drischler, C., Soma, V., & Schwenk, A. 2014, PhRvC, 89, 025806
Dyhdalo, A., Furnstahl, R. J., Hebeler, K., & Tews, I. 2016, PhRvC, 94, 034001
Ecker, C., Hoyos, C., Jokela, N., Rodríguez Fernández, D., & Vuorinen, A. 2017, JHEP, 1711, 031
Epelbaum, E., Hammer, H. W., & Meissner, U. G. 2009, RvMP, 81, 1773
Epelbaum, E., Krebs, H., & Meiner, U. G. 2015, EPJA, 51, 53
Fraga, E. S., Kurkela, A., & Vuorinen, A. 2016, EPJA, 52, 49
Gal, A., Hungerford, E. V., & Millener, D. J. 2016, RvMP, 88, 035004
Gandolfi, S., Carlson, J., & Reddy, S. 2012, PhRvC, 85, 032801
Gandolfi, S., Gezerlis, A., & Carlson, J. 2015, ARNPS, 65, 303
Gezerlis, A., Tews, I., Epelbaum, E., et al. 2013, PhRvL, 111, 032501
Gezerlis, A., Tews, I., Epelbaum, E., et al. 2014, PhRvC, 90, 054323
Glendenning, N. K. 1982, PhL, 114B, 392
Hagen, G., Papenbrock, T., Ekström, A., et al. 2014, PhRvC, 89, 014319
Hambaryan, V., Suleimanov, V., Haberl, F., et al. 2017, A&A, 601, A108
Hebeler, K., Holt, J. D., Menendez, J., & Schwenk, A. 2015, ARNPS, 65, 457
Hebeler, K., Lattimer, J. M., Pethick, C. J., & Schwenk, A. 2013, ApJ, 773, 11
Hebeler, K., & Schwenk, A. 2010, PhRvC, 82, 014314
Holt, J. W., & Kaiser, N. 2017, PhRvC, 95, 034326
Hoyos, C., Jokela, N., Rodríguez Fernández, D., & Vuorinen, A. 2016, PhRvD, 94, 106008
Huth, L., Tews, I., Lynn, J. E., & Schwenk, A. 2017, PhRvC, 96, 054003
Koranda, S., Stergioulas, N., & Friedman, J. L. 1997, ApJ, 488, 799
Krüger, T., Tews, I., Hebeler, K., & Schwenk, A. 2013, PhRvC, 88, 025802
Kurkela, A., Fraga, E. S., Schaffner-Bielich, J., & Vuorinen, A. 2014, ApJ, 789, 127
Kurkela, A., Romatschke, P., & Vuorinen, A. 2010, PhRvD, 81, 105021
Lattimer, J. M., & Prakash, M. 2005, PhRvL, 94, 111101
Lim, Y., & Holt, J. W. 2018, arXiv:1803.02803
Lonardoni, D., Lovato, A., Gandolfi, S., & Pederiva, F. 2015, PhRvL, 114, 092301
Lynn, J. E., Tews, I., Carlson, J., et al. 2016, PhRvL, 116, 062501
Lynn, J. E., Tews, I., Carlson, J., et al. 2017, PhRvC, 96, 054007
Machleidt, R., & Entem, D. R. 2011, PhR, 503, 1
Margueron, J., Hoffmann Casali, R., & Gulminelli, F. 2018, PhRvC, 97, 025806
Miller, M. C. 2016, ApJ, 822, 27
Most, E. R., Weih, L. R., Rezzolla, L., & Schaffner-Bielich, J. 2018, arXiv:1803.00549
Moustakidis, C. C., Gaitanos, T., Margaritis, C., & Lalazissis, G. A. 2017, PhRvC, 95, 045801
Ozel, F., & Freire, P. 2016, ARA&A, 54, 401
Paeng, W. G., & Rho, M. 2016, arXiv:1611.09975
Raithel, C. A., Ozel, F., & Psaltis, D. 2016, ApJ, 831, 44
Reardon, D. J., Hobbs, G., Coles, W., et al. 2016, MNRAS, 455, 1751
Sammarruca, F., Coraggio, L., Holt, J. W., et al. 2015, PhRvC, 91, 054311
Steiner, A. W., & Gandolfi, S. 2012, PhRvL, 108, 081102
Steiner, A. W., Gandolfi, S., Fattoyev, F. J., & Newton, W. G. 2015, PhRvC, 91, 015804
Steiner, A. W., Heinke, C. O., Bogdanov, S., et al. 2018, MNRAS, 476, 421
Tews, I. 2017, PhRvC, 95, 015803
Tews, I., Gandolfi, S., Gezerlis, A., & Schwenk, A. 2016, PhRvC, 93, 024305
Tews, I., Krüger, T., Hebeler, K., & Schwenk, A. 2013, PhRvL, 110, 032504
Tews, I., Margueron, J., & Reddy, S. 2018, arXiv:1804.02783
Wlazowski, G., Holt, J. W., Moroz, S., Bulgac, A., & Roche, K. J. 2014, PhRvL, 113, 182503